# Reference Cell Performance and Modeling on a One-Axis Tracking Surface

## Preprint

Frank Vignola,[1] Josh Peterson,[1] Rich Kessler,[1]
Sean Snider,[2] Peter Gotseff,[3] Manajit Sengupta,[3]
Aron Habte,[3] Afshin Andreas,[3] and Fotis Mavromatakis[4]

*1 University of Oregon*
*2 St. Mary's High School*
*3 National Renewable Energy Laboratory*
*4 Hellenic Mediterranean University*

*Presented at the IEEE Photovoltaic Specialists Conference (PVSC)*
*Philadelphia, Pennsylvania*
*June 5–10, 2022*

**NREL is a national laboratory of the U.S. Department of Energy**
**Office of Energy Efficiency & Renewable Energy**
**Operated by the Alliance for Sustainable Energy, LLC**

This report is available at no cost from the National Renewable Energy Laboratory (NREL) at www.nrel.gov/publications.

Contract No. DE-AC36-08GO28308

**Conference Paper**
NREL/CP-5D00-82061
December 2022

# Reference Cell Performance and Modeling on a One-Axis Tracking Surface

## Preprint

Frank Vignola,[1] Josh Peterson,[1] Rich Kessler,[1]
Sean Snider,[2] Peter Gotseff,[3] Manajit Sengupta,[3]
Aron Habte,[3] Afshin Andreas,[3] and Fotis Mavromatakis[4]

*1 University of Oregon*
*2 St. Mary's High School*
*3 National Renewable Energy Laboratory*
*4 Hellenic Mediterranean University*

**Suggested Citation**
Vignola, Frank, Josh Peterson, Rich Kessler, Sean Snider, Peter Gotseff, Manajit Sengupta, Aron Habte, Afshin Andreas, and Fotis Mavromatakis. 2022. *Reference Cell Performance and Modeling on a One-Axis Tracking Surface: Preprint*. Golden, CO: National Renewable Energy Laboratory. NREL/CP-5D00-82061.
https://www.nrel.gov/docs/fy23osti/82061.pdf.



**NREL is a national laboratory of the U.S. Department of Energy**
**Office of Energy Efficiency & Renewable Energy**
**Operated by the Alliance for Sustainable Energy, LLC**

This report is available at no cost from the National Renewable Energy Laboratory (NREL) at www.nrel.gov/publications.

Contract No. DE-AC36-08GO28308

**Conference Paper**
NREL/CP-5D00-82061
December 2022

National Renewable Energy Laboratory
15013 Denver West Parkway
Golden, CO 80401
303-275-3000 • www.nrel.gov

**NOTICE**

This work was authored in part by the National Renewable Energy Laboratory, operated by Alliance for Sustainable Energy, LLC, for the U.S. Department of Energy (DOE) under Contract No. DE-AC36-08GO28308. Funding provided by the U.S. Department of Energy Office of Renewable Energy and Energy Efficiency Solar Energy Technologies Office. The views expressed herein do not necessarily represent the views of the DOE or the U.S. Government.

# Reference Cell Performance and Modeling on a One-Axis Tracking Surface

Frank Vignola[1], Josh Peterson[1], Rich Kessler[1], Sean Snider[2], Peter Gotseff[3], Manajit Sengupta[3], Aron Habte[3], Afshin Andreas[3], and Fotis Mavromatakis[4]

[1]Material Science Institute/University of Oregon, Eugene, Oregon, 97403 (USA)

[2]St. Mary's High School, Medford, Oregon, 97504, (USA)

[3]National Renewable Energy Laboratory, Golden, Colorado, 80401 (USA)
[4]Department of Electrical and Computer Engineering/Hellenic Mediterranean University, Heraklion 71004 Crete Greece

***Abstract*—Performance of five silicon-based reference cells is examined on a single-axis tracking surface. The reference cells' output are modeled using one-minute sampled spectral irradiance and reference cell temperature measurements. The model also incorporates spectral responsivity data for the reference cell. The transmission of light through the glazing multiplies the sum over all appropriate wavelengths of temperature adjusted reference cell responsivity times the measured spectral irradiance. Modeled reference cell output is compared with measured reference cell output under clear sky and totally cloudy sky conditions. For each reference cell the ratio of modeled to measured output varies by less than 2% over the year.**

***Keywords*—*Solar Reference Cells, Spectral Irradiance, Modeling***

## I. Introduction

Reference cells can be used to monitor and evaluate the performance of photovoltaic systems in the field because they have spectral and transmission characteristics similar to photovoltaic modules. Thermopile-based pyranometers are excellent instruments used to measure incident radiation in the field and are minimally affected by changes in the distribution of incident spectral irradiance and by the angle-of-incidence (*AOI*) of incoming irradiance. To estimate photovoltaic system performance using data from pyranometers, the spectral and angle-of-incidence effects seen by photovoltaic modules have to be modeled. Many models and programs have been developed and tested to estimate photovoltaic system performance using irradiance data. To estimate incident radiation with reference cells for comparison to irradiance estimates from satellites or for use at different tilts and orientations, models are needed to translate the reference cell measurements into irradiance values.

The overarching goal of this project is to understand, characterize, and evaluate the measurements from reference cells so that they can be used to produce useful estimates of the incident irradiance and build confidence in reference cell measurements for the analysis of photovoltaic (PV) system performance. To avoid introducing systematic biases inherent in pyranometer measurements into irradiance estimates from reference cells, a model was developed and is being tested to emulate the measurements of reference cells. Once confidence in the model is established, the model components can then be used to estimate the incident irradiance and the uncertainties in the irradiance estimates from reference cells.

The three main factors affecting the modeling of reference cells are:

1. Dependence on the incident spectral distribution,
2. Effect of transmission of light through the glazing (angle-of-incidence effects), and
3. Influence of reference cell temperature on the output values.

In previous studies, [1, 2, 3] the output of reference cells on a two-axis tracking surface was modeled using measured spectral irradiance and the temperature of the reference cells. The use of the two-axis tracking surface minimized the angle-of-incident effects on the measurements. Since the temperature effects are small, the study on the two-axis tracking surface enabled testing the importance of the spectral irradiance distribution on the output of reference cells. The current study expands the original analysis by studying the output of five different reference cells and evaluating the performance on a one-axis tracking surface. The angle-of-incident effects become important because, on a one-axis tracking surface, the angle-of-incidence varies considerably over the day and over the year.

The instruments used in the experiment are discussed first. Then the model used to emulate the performance of reference cells is described. Next the relationship between the reference cell and model output is evaluated. After examining the magnitude of different components of the model, a summary of results is presented along with a discussion of next steps.

## II. Experimental Setup

The equipment used in this experiment are located at the Solar Radiation Research Laboratory (SRRL) in Golden, Colorado. Fig. 1 is a photograph of the EKO one-axis tracker with the pyranometers, reference cells, and spectroradiometers.

Mounted on the platform are the EKO Weiser spectroradiometer, a Kipp & Zonen CMP 22 pyranometer along with an SP-Lite 2, a Li-Cor pyranometer, and five reference cells. The reference cells are:

1. Atonometrics (ATO)
2. EETS (EET)
3. IKS Photovoltaik (IKS)
4. IMT (IMT)
5. NES (NES)

Fig. 1. Experimental setup at SRRL in Golden, Colorado. Photo from NREL.

These mono-crystalline reference cells were calibrated at the NREL Cell Lab under a standard lamp perpendicular to the reference cell. The factory calibrations were used in the experiment. The lab calibration have a 0.9% uncertainty at the 95% level of confidence [4]. Most of the lab calibrations were 0.8% lower than the factory calibrations, but the lab calibration for the EET calibration was 1.0% higher than the factory calibration value. These values fall within the range of uncertainties of 1.4% - 3.0% quoted by the manufacturers.

The spectral responsivity of the reference cells were derived from the quantum efficiency values measured at the NREL Cell Lab for each reference cell. Spectral responsivities were then calculated and normalized to 1 at the peak response wavelength. Because the spectral responsivities were relative values, a scale factor has to be determined for each reference cell.

## III. Model Description

The model proposes that the measured output of the reference cell (*RC*) is proportional to the average transmission of light through the glazing times the sum over all wavelengths of the reference cell spectral responsivity *R(T)* adjusted for temperature times the incident radiation $I_\lambda$ (1).

Because the spectral responsivity is a relative value a calibration constant, *K*, is need to produce an output value. This is similar to the responsivity used to determine the output of a pyranometer. The reference cell (*RC*) output is modeled by the right side of (1).

$$RC_{model} = F(AOI)/K \cdot \sum_{\lambda=280nm}^{4000nm} R_\lambda(T) \cdot I_\lambda \qquad (1)$$

where *F(AOI)*, the average transmission of light through the reference cell glazing, is determined using the Marion model [5] and the broadband beam and diffuse components of the incident radiation. In this model, *F(AOI)* is assumed to be independent of wavelength. The scaling factor, *K*, relates the model estimates to the measured values. The scaling factor is needed because the spectral responsivities are relative values and not absolute values.

The model uses the reference cell spectral response, $R_\lambda(T)$, determined from the reference cell normalized quantum efficiency adjusted for the measured reference cell temperature, *T*. The adjustment to the spectral responsivity $R_\lambda(T)$ was determined using the Hishikawa model [6]. For wavelengths below the peak wavelength, the spectral responsivity was not adjusted. For wavelength above the peak wavelength, the spectral responsivity was assumed to be the spectral responsivity of the wavelength of $\lambda$ plus a shift. The shift was calculated using (2).

$$Shift = 0.45 \cdot (T - 25) \qquad (2)$$

*Shift* values are rounded to the nearest one nm. A factor of 0.45 times the difference between the reference cell temperature and 25C was used to emulate the shift suggested by Hishikawa [6] for single crystalline silicon. For example, if the reference cell temperature was 45C, then the *Shift* would be 9 nm and the spectral responsivity at 1000 nm would be give the value of the reference cell responsivity at 991 nm.

The spectral irradiance, $I_\lambda$, is measured at one-nm wavelengths from 350 nm to 1650 nm using an EKO Weiser spectroradiometer mounted on the one-axis tracker. The EKO Weiser spectroradiometer used on the one-axis tracker consists of two spectroradiometers one of which measures wavelengths from 350 nm to 1100 nm and another that measures wavelengths from 900 nm to 1650 nm. The wavelengths values from 900 nm to 1100 nm are determined from algorithms using measurements from both instruments. Spectral intensity from 300 nm to 350 nm was estimated using a linear fit between 0 $Wm^{-2}$ at 300 nm to the measured irradiance at 350 nm.

To obtain the angle-of-incidence function, the incident radiation is separated into the beam irradiance and diffuse irradiance components on the one-axis tracking surface. The various diffuse components are obtained from the Perez model [8]. The diffuse irradiance is separated into circumsolar, dome, horizon, and ground reflected components. The transmission of light through the glazing *F(AOI)* of the various irradiance components were obtain from Marion model [5].

Five reference cells were compared, the ATO, IMT, IKS, EET, and NES. These are all monocrystalline reference cells and factory calibration values were used to obtain measured output.

For a one-axis tracker, the tilt of the tracker is given by (3) where *SZA* and *AZM* are the solar zenith angle and the azimuthal angle of the sun respectively [7]

$$Tilt = \tan^{-1}[\tan(SZA) \cdot \sin(AZM - 180)] \qquad (3)$$

The angle-of-incidence ($AOI$) is given in (4)

$$AOI = \cos^{-1}[-\sin(SZA)\sin(AZM) \cdot \sin(Tilt) + \cos(SZA) \cdot \cos(Tilt)] \quad (4)$$

## IV. Results

An initial evaluation of the modeled and measured output of the EET reference cell is shown in Fig. 2, a plot of reference cell output verses angle-of-incidence ($AOI$). The plot is shown for the clear day of September 12, 2020. The left vertical axis is the measure reference cell output and the right vertical axis is the modeled reference cell output. The reference cell obtained its calibration from the factory. Since the model components do not have an established calibration methodology, the output from the reference cell has to serve to determine the calibration factor ($K$). The scale on the right hand axis is 0.56 time the scale on the left hand axis and this gives a first estimate of the model's calibration factor.

To evaluate the relationship between the measured and modeled values, a more detailed examination is done by looking at the ratio of the modeled and measured output of the reference cell, see Fig. 3. This ratio yields the calibration factor $K$ from (1). Because there was no well-defined method to obtain field calibration values that relate reference cell output to broadband irradiance, the $K$ are specific to the reference cell and the factory calibration value used. If a standard calibration methodology is obtained for reference cells, then a more defined specification for $K$ values can be obtained.

One-minute data was used and sample results from all five reference cells are plotted in Fig. 3 for September, 12, 2020. Although the $K$ ratios differ by about 4%, they have similar patterns over the day.

To give a common reference point, the $K$ factors for the reference cells were normalized to the EET reference cells at a solar zenith angle of 45° on September 12, 2020. For each type of reference cell, the normalization factor (NF) was calculated from the ratio of the K factors at a SZA of 45° on September 12, 2020 (5).

$$NF = K(RC, 45°)/K(EET, 45°) \quad (5)$$

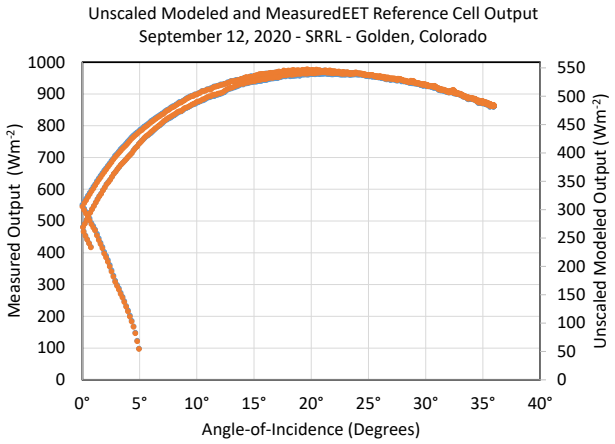


Fig. 2. Unscaled modeled output and measured output of an EET reference cell on a sunny day, Sept. 12, 2020. Vertical scale on left is for the measure RC output and the vertical scale on the right is for the unscaled modeled RC output.

where the normalization factor ($NF$) multiplies all the $K$ factors for reference cell type $RC$.

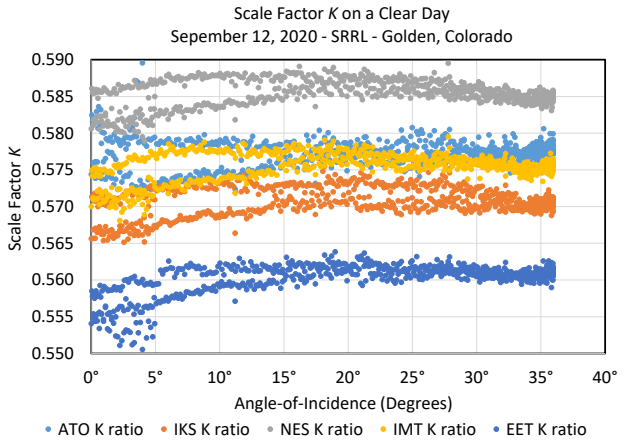


Fig. 3. Scaling factor, $K$, needed to equate modeled reference cell output to measured reference cell output on a one-axis tracking surface. 9/12/2020

In doing this, plot of $K'$ factors, K factor multiplied by the ratio, for all reference cells show them almost falling on top of each other and exhibit 1% spread over the day. This 1% spread over the day is typical of the individual $K$ values in Fig. 3. For most of the day, the values are within 1% of the noontime value. Each modeled reference cell shows a small split in the $K$ values determined in the morning and afternoon as a function of $AOI$.

To evaluate if the results observed on September 12, 2020 are consistent throughout the year, Fig. 4 and 5 plot the $K'$ factor for the clear day on July 1, 2020 and December 25, 2020. This is an attempt to discuss universal characteristics of $K$ values, the ratios were normalized to the EET ratio at a solar zenith angle of 45° on September 12, 2020. The goal of the normalization is to help provide a visual basis for the discussion of the uncertainties and biases of the model and minimize the differences caused by different calibration methodologies.

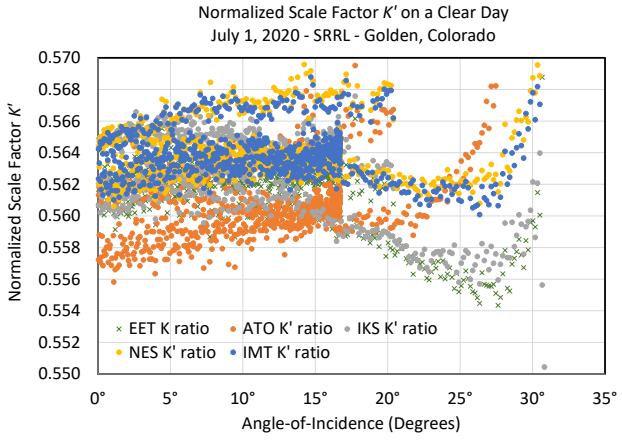


Fig. 4. Normalized scale factor $K'$ relating modeled output to the measured output on a one-axis tracking surface. $K$ factors were normalized using the value that made all reference cells agree with the EET output on 9/12/2020 at a SZA of 45°.

In Fig. 4, the difference between the various reference cells is about 1.7% over the day. Some of this difference is brought about by the lower values of the normalized ATO *K* values. *AOI* greater than 20° correspond to early morning values. The patterns are different for groups of reference cells and the source of this difference has not been identified.

In Fig, 5, a similar clear sky plot is obtained for December 25, 2020. The spread in *K* values is about 2% at the largest *AOI*s. The largest *AOI* values occur at this time of year when the one-axis tracking surface is near the horizontal position. Near solar noon, there is a peak in the *K* values. As opposed to the data in Fig. 4, the ATO *K* values in Fig. 5 are now larger than the other *K* values.

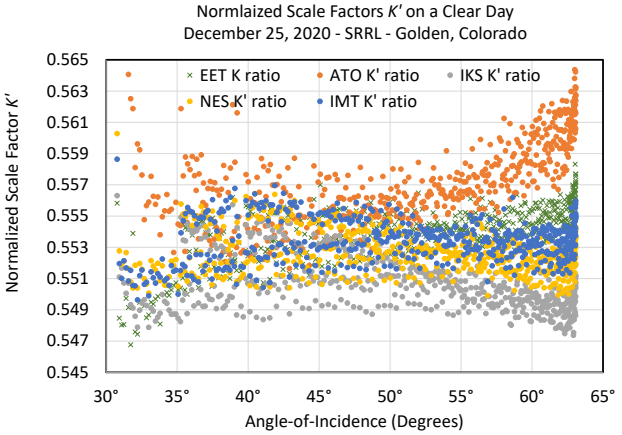


Fig. 5. Normalized scale factor relating modeled output to the measured output on a one-axis tracking surface. *K* factors were normalized using the value that made all reference cells agree with the EET output on 9/12/2020 at a SZA of 45°.

To examine the changes in behavior over the year, Fig. 6 plots the clear sky values of the reference cells over the 2020 through 2021 time period. The clear sky values were determined by comparing the clear sky models for global horizontal irradiance (GHI) against measured GHI values and using percent cloudiness values of 15% or less. In addition direct normal irradiance (DNI) values were used to help insure the skies were not significantly affected by thin clouds.

The NES reference cells shown in Fig. 6 exhibit a 2% difference in the ratio *K* over the year. The ATO reference cells exhibit smaller change over the year, but have about a 2% variation over the day. These examples are typical of other reference cells studied. The sinusoidal variation over the year is under investigation.

In Fig. 7, the performance of the NES reference cells over totally cloudy periods is studied. For the model to be most useful, it has to work under all sky conditions. It is difficult to make comparisons over partially cloudy skies because the irradiance can vary significantly over short intervals and spectral measurements are made over a short time span (one to five seconds). To counter this, sample reference cell measurements were used instead of minute averages. This is fine for clear sky comparisons, but is difficult for partially cloudy skies because timing issues of when measurements were made and when clouds affect a sensor become important.

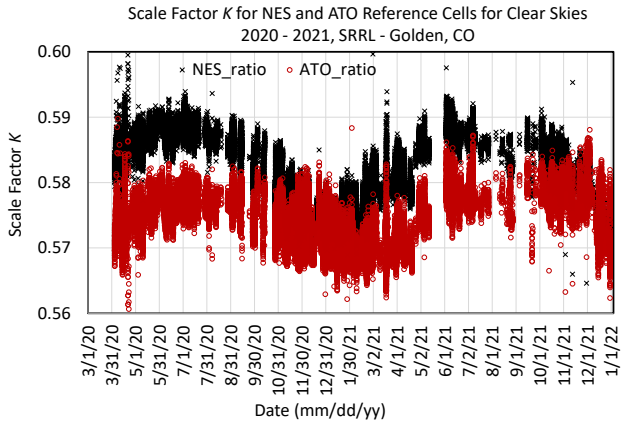


Fig. 6. Scale factor *K* relating modeled to measured output for NES (x) and ATO (o) reference cells for 2020 and 2021 on a one-axis tracking surface. *K* has a peak in summer and a minimum in winter. This is about a 2% difference over the year.

Therefore total cloudy skies are studied. For the data from SRRL, periods where cloud cover were greater than 75% and DNI measurements of less than 100 $Wm^{-2}$ were selected.

*K* varies about 4% on cloudy days and doesn't show a marked trend over the year. Some of the variation shown in Fig.7 results from other factors such as maintenance or problems with other instruments. The ratios for the NES instrument are typical of plots for other instruments over the year.

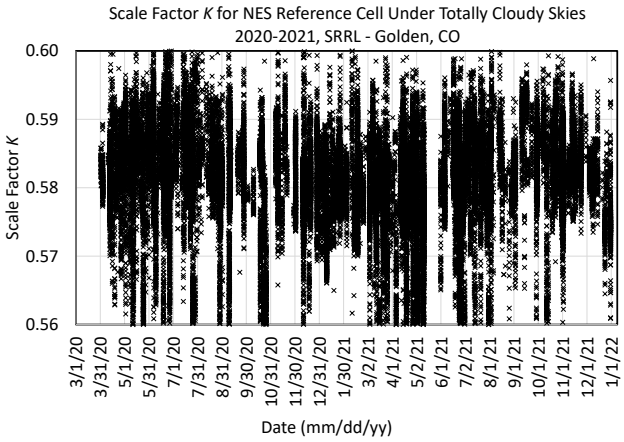


Fig. 7. Scale factor *K* relating modeled to measured output for a NES reference cell on a one-axis tracking surface for 2020 under totally cloudy skies.

### *A. Discussion of Results*

The average values of the *K* factors over year has been calculated using the average *F(AOI)*s and the sum of the reference cell spectral responsivity times incident spectral irradiance and dividing by the reference cell measurement. This is based on the assumption that the modeled reference cell output is equal to the measured reference cell output once the scale factor, *K* has been determined. The comparison between the model estimates and the measured reference measurements agree to better than 2% as illustrated in Figs. 2 to 7. Is this

difference a limitation of the model or is the variation associated with the measurements? The next subsections look at some of the possible sources of biases associated with the various model components.

### 1) *Uncertainties associated with temperature measurements*

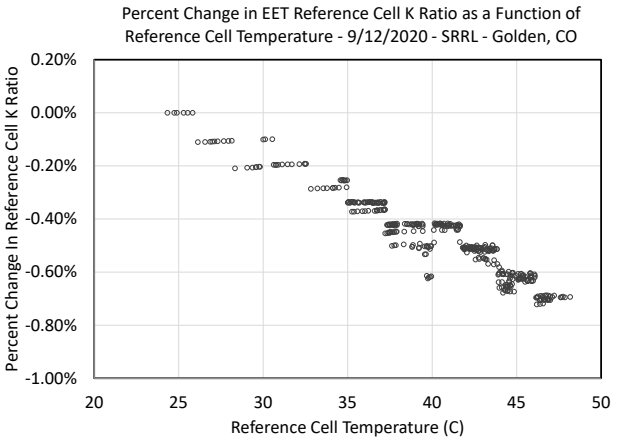


Fig. 8. Study of the effect of the temperature adjustment on the ratio of modeled to measured reference cell output on September 12, 2020. The plot is $(K_{WithoutTemperature} - K_{WithTemperature})/K_{WithTemperature}$.

To start, the influence temperature measurements in the temperature adjustment is examined. With PV systems, temperature is important but with reference cells, the temperature dependence is minimal because the measurements are made using short circuit current which has minimal dependence on temperature. A quick estimate of the importance of temperature can be obtained by examining the difference between the modeled *K* values with and without an adjustment for temperature. Fig. 8 plots the difference between *K* values with and without the temperature adjustment. This plot is showing that as an extreme, the overall change in the *K* value as a function of temperature is about 0.03% per degree C or about 0.7% over the 20C range.

With the estimate of the dependence of *K* on temperature, one can estimate the uncertainty introduced to the results by the uncertainty in the temperature measurement. There is a significant difference in temperature measurements between reference cells. On a sunny day, the temperature difference between the hottest and coldest reference cell can be 10C or more with the standard deviation between all reference cells about 5C. If one assumes a 5C uncertainty in the temperature measurement, this translate into 0.15% uncertainty in *K*.

In addition to the difference between measured temperature of individual reference cells, reference cell temperatures sometimes vary from one minute to the next. This can either be related incident radiation, wind speed, or stability of the temperature measurement. A plot of IMT reference cell temperature is shown in Fig. 9 alongside a plot of IMT output. The IMT output is fairly consistent and the temperature of the reference cells can vary by as much as 10C in a manner of minutes. From Fig. 8, a 10C difference would amount to about a 0.3% change in the *K* ratio. This temperature variation adds to the variation of the *K* values obtained.

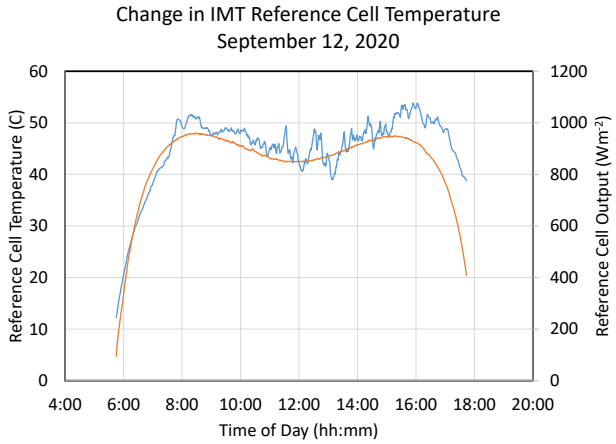


Fig. 9. Variation in the IMT reference cell temperature over the day on September 12, 2020. Also plotted in the IMT reference cell output. Wind speed varies from 2 m/s to 3 m/s over the day.

### 2) *Uncertainties associated with F(AOI)*

The uncertainty in the amount of light transmitted through the glazing is dependent on the angle-of-incidence and the irradiance, the *F(AOI)* for DNI is 1. The *F(AOI)s* for the various irradiance components are plotted against *AOI* on September 12, 2020 in Fig.10.

As shown in Fig. 10, diffuse radiation from the dome is fairly constant over the day and is about 0.96. The circumsolar transmission factor is close to 1 and decreases slightly as the *AOI* increases. When the tracker is horizontal, the angle-of-incidence for the horizon irradiance and the ground reflected irradiance is ~90 degrees. At these *AOI* values, 37° on 9/12/2020, the modeled horizon and ground reflected *F(AOI)* goes to zero. This is an approximation for the horizon brightening as the horizon brightening is actually slightly above the horizon. Both the horizon brightening transmission and the ground reflected transmission increase significantly as the surface tilts and the average *AOI* of the surface decreases relative magnitudes of the direct, diffuse, and ground reflected irradiance. For a surface perpendicular to the incident beam, the

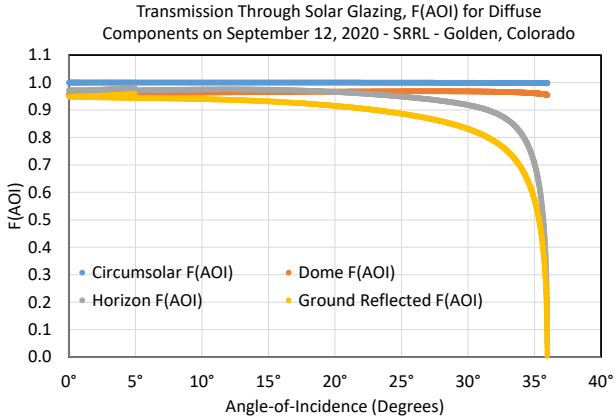


Fig. 10. Transmission through a solar glazing for various diffuse components [8] as a function of *AOI* on 9/12/2020.

average *F(AOI)* is obtained by weighing the *F(AOI)*s times the magnitude of the irradiance components. On a clear day in September, the average *F(AOI)* varies from close to 1 to 0.9945 under clear skies, see Fig. 11. The average *F(AOI)* is dominated by the beam and circumsolar irradiance that have *F(AOI)*s close to 1. The sharp decrease in average *F(AOI)* at an *AOI* around 37° is the result of the rapid rise in the ground and horizon brightening *F(AOI)*s combined with the sudden addition of these irradiance components to the total diffuse irradiance. The modeled average *F(AOI)* drops from above 0.997 to slightly below 0.995. For an *AOI* about 35° and the rise in the horizon and ground reflected starts to moderate and the relationship between average *F(AOI)* and *AOI* becomes more linear. The morning and afternoon average *F(AOI)* differ because the relative magnitude of DNI and the diffuse irradiance is different.

Also shown in Fig. 11 is the average *F(AOI)* for December 25, 2020. At larger *AOI*s, near solar noon, less light is transmitted through the glazing and in December, the *AOI* values are much larger than September and the transmission of light is less. For the clear day on December 25, 2020, *F(AOI)* varies from 0.998 near sunrise to 0.947 at noon. Therefore, any biases associated with *F(AOI)* are most important in the winter months when the *AOI* become greater than 40° to 45°.

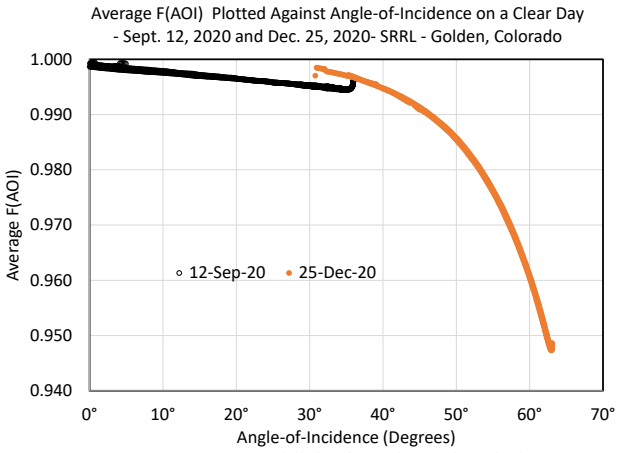


Fig. 11. Average transmission of light through a solar glazing, *F(AOI)*, plotted against angle-of-incidence – September 12, 2020 and December 25, 2020. Different proportions of DNI and DHI values account for the differences in *F(AOI)* between 30° and 37°

### *3) Biases in estimating the diffuse components*

There are also biases associated with separating the diffuse radiation into the diffuse components. Separating the diffuse components and projecting them onto a one-axis tracking surface offers a unique test of the Perez model [8] that separates the irradiance into the diffuse and ground reflected components. The orientation of the surface varies over the day resulting in many orientations not usually experienced.

The modeled diffuse components on a one-axis tracking surface under clear skies on September 12, 2020 are shown in Fig. 12. The components were calculated using the Perez model [8] with the tilt and orientation calculated each minute. The calculated total diffuse on a one-axis tracking surface is about

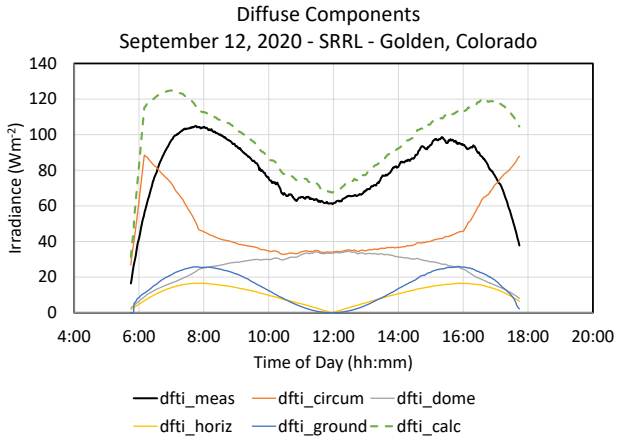


Fig. 12. Diffuse and ground reflected components on September 12, 2020. Solid black line is the diffuse irradiance obtained by subtracting DNI projected onto a one-axis tracking surface from the measured GTI. The dashed green line is the sum of the diffuse and ground reflected components on a one-axis tracking surface.

10 $Wm^{-2}$ higher than the "measured" diffuse for much of the day. However, the modeled diffuse overestimates the diffuse from the measured data in the morning and afternoon hours.

The diffuse components for December 25, 2020 are plotted in Fig. 13. The 25th was chosen because it was a clear day with minimal snow cover on the ground. At solar noon, the measured and calculated diffuse irradiance are within 10 to 15 $Wm^{-2}$ of each other. In the morning, during the clearest part of the day, the difference between the measured and calculated total diffuse is the largest. At solar noon when the one-axis tracking surface is horizontal, the GTI measurements is about 10 $Wm^{-2}$ below other diffuse measurements at SRRL. This is within the specifications of the pyranometer. However, this doesn't explain the larger differences in the morning. The probable cause for this difference is the overestimate of one or more of the diffuse components. One possibility is that the circumsolar diffuse irradiance is assumed to be evenly distributed around

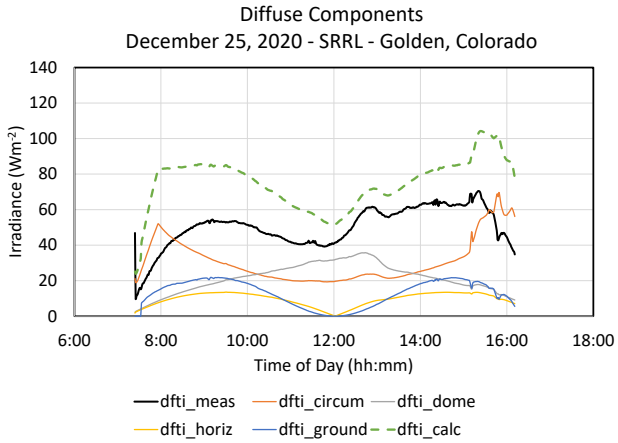


Fig. 13. Diffuse and ground reflected components on December 25, 2020. Solid black line is the diffuse irradiance obtained by subtracting DNI projected onto a one-axis tracking surface from the measured GTI. The dashed green line is the sum of the diffuse and ground reflected components on a one-axis tracking surface.

the sun. When the sun is low on the horizon as during the winter or near sunrise or sunset, some of this circumsolar may be obscured by the horizon. Modeling of the reference cell output might be improved with a better understanding of how to separate the diffuse irradiance into it various components.

*4) Influence of biases in the diffuse components*

The average *F(AOI)* is dependent upon the relative magnitudes of the beam and diffuse components on the tilted surface. The average diffuse *F(AOI)* was obtained by averaging the product of the modeled diffuse components times the *F(AOI)* for each component (6). To minimize the bias that results from the difference between the sum of the diffuse tilted components and the measured tilted diffuse, the sum of the modeled *DfTI* component, $DfTI_{calculated}$, was used to obtain the $F(AOI)_{avgdiff}$.

$$F(AOI)_{avgdiff} = [DfTI_{circumsolar} \cdot F(AOI)_{circum} + DfTI_{dome} \cdot F(AOI)_{dome} + DfTI_{horizon} \cdot F(AOI)_{horizon} + GRI_{ground} \cdot F(AOI)_{ground}] / DfTI_{calculated} \quad (6)$$

where $F(AOI)_{avgdiff}$ is the average of the tilted diffuse components. The diffuse components on the tilted surface are $DfTI_{circumsolar}$ the diffuse circumsolar component, $DfTI_{dome}$ the diffuse dome component, $DfTI_{horizon}$ the diffuse horizon brightening component, and $GRI_{ground}$ the ground reflected component. A similar naming convention applies to the *F(AOI)* components.

The average $F(AOI)_{avg}$ for all irradiance is given by combining the beam with the diffuse components (7).

$$F(AOI)_{avg} = [DfTI_{meas} \cdot F(AOI)_{avgdiff} + DNI \cdot \cos(AOI) \cdot F(AOI)_{circum}] / GTI \quad (7)$$

where *GTI* is the total measured irradiance on a one-axis tracking surface. When $F(AOI)_{avg}$ is calculated, $F(AOI)_{avgdiff}$ is multiplied by the $DfTI_{meas}$, the diffuse value obtained by subtracting *DNI* projected onto the tilted surface from *GTI* (8).

$$DfTI_{meas} = GTI - DNI \cdot \cos(AOI) \quad (8)$$

Obtaining $DfTI_{meas}$ using (8) is another source of uncertainty because the measured *GTI* and *DNI* also have well characterized uncertainties and biases that increase the uncertainty in $DHI_{meas}$ obtained this way. Uncertainties in the $DfTI_{meas}$ can be ±10 to 20 $Wm^{-2}$.

Evaluating (7), the uncertainty in $DHI_{meas}$ only becomes important if $F(AOI)_{avgdiff}$ is much less than one. Since, under clear skies, the average *F(AOI)*s on a one-axis tracking surface change very little except during the winter months. The relative difference between the modeled diffuse components and $DHI_{meas}$ aren't significant. The same cannot be said for the winter months, when the *AOI* is large and the individual diffuse components have greater influence on $F(AOI)_{avg}$.

## V. Significance of Findings

The proposed reference cell model uses spectral and temperature measurements, spectral responsivity data for the reference cell, and broadband irradiance measurements. The model estimates of the reference cell output to within 1% to 2% of measure reference cell output. This information should be sufficient to estimate the incident irradiance being measured by the reference cell. Two critical pieces of information are missing before practical use of this model can be made. First, a definition of standard conditions is needed along with a quantified methodology for calibrating the reference cell.

To illustrate the need for standard conditions, a comparison between the measured reference cell output and measured *GTI* on a one-axis tracking surface using a Kipp & Zonen CMP 22 pyranometer is shown in Fig. 14. The range of differences between reference cell measurements and the high quality pyranometer readings range from +6% to -4% with some reference cells experiencing a smaller range. By taking into account the transmission of irradiance through the glazing, the temperature of the reference cell, and the changing spectral irradiance over the day, it is possible to significantly reduce this difference. First the reference cells needs to be calibrated using a standard methodology. Under these conditions, a direct link between reference cell output and incident radiation would be obtained. Using the data and model under these conditions, the model's *K* value can be determined. Currently there is an ambiguity here and similar reference cells produce different values under identical conditions, see Fig. 3.

This study has shown how the reference cell measurements are dependent on the incident spectral irradiance, the transmission of light through the glazing, and the reference cell temperature. As the conditions experienced by the reference cell in the field move away from the standard conditions, the relationship between irradiance and reference cell output changes. The changing relationship between "measured" *GTI* and reference cell output is shown in Fig. 14. The *GTI* measurements are from a CMP 22 pyranometer that also has some dependence on conditions under which the measurement were made. However, these are small compared to the dependences (systematic biases) of the reference cells. Knowing the dependencies of the reference cell to changing conditions can be taken into account and it is possible to make adjustments to the reference cell output to obtain better estimates of incident radiation. This is similar to adjustments

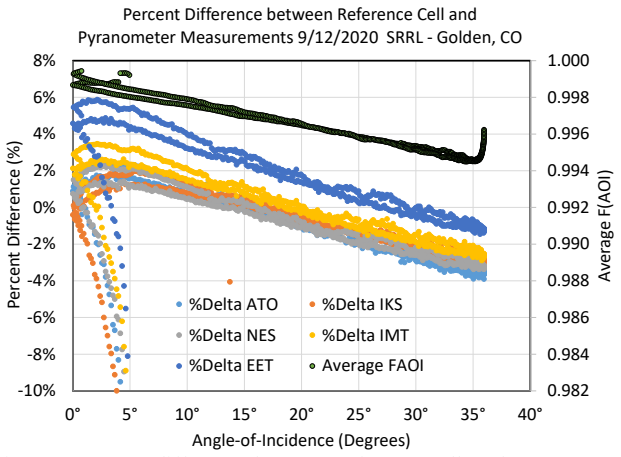


Fig. 14. Percent difference between reference cell and pyranometer measurements (CMP 22) on a one-axis tracking surface on September 12, 2020. The scale for the average F(AOI) is the right hand axis. Factory calibrations were used for the reference cell measurements.

made to rotating shadowband radiometers to obtain better estimates of beam and diffuse irradiance.

The methodology used in this study should enable reliable estimates of irradiance. In practice, the spectral irradiance would have to be modeled instead of measured because spectral irradiance measurements are rarely available. This spectral modeling needs testing. More work is necessary to validate the model and determine how well irradiance values can be obtained from reference cell measurements. The spread of reference cell outputs is an example of this issue. Once standard conditions and calibrations are obtained, it is possible to compare pyranometer readings and reference cell measurements by reducing the systematic biases of the reference cell biases from the measurements.

Figs. 3 through 6, illustrate that it is possible to model the conditions that result in the reference cell measurements to within 1% to 2% of the reference cell output. By normalizing the reference cell output to standard conditions it should be possible to specify the reference cell output under those conditions. Under the standard conditions, the reference cell is calibration to match the incident broadband irradiance. The normalized reference cell output would give a much better estimate to the incident radiation.

It is important to evaluate results from different locations and on a horizontal or fixed tilted surfaces. So far the model has only been tested with *AOI* up to 60°. The *F(AOI)* for *AOI* between 60° and 90° are expected to change significantly and these angles have not been tested in this data. Different locations are also expected to expand the sky conditions being tested and are needed to help insure the universal applicability of the model.

Pyranometers measurements have their own set of uncertainties and systematic biases as do reference cell measurements. The uncertainties and biases associated with pyranometer measurements are well defined and procedures to obtain the uncertainty values are well established. If reference cells measurements are to be compared with pyranometer measurements, calibration procedures and methodology for reference cells have to be established. The model used to emulate the performance of reference cells provides some guidance on information that needs to be taken into account. The uncertainties incorporated in the model need to be better defined and explored. The uncertainties introduced by the various components of the model need to be determined. This is not easy even with well-defined calibration procedures.

The small uncertainties obtained during this study are dependent on the spectral irradiance measurements. If the spectral irradiance is modeled, then the uncertainties will increase because there are larger uncertainties in models spectral values. This is an aspect for future work.

Overall, the goal has been to produce useful results that will improve the understanding and performance estimates of photovoltaic systems. The model replicates the performance of reference cells and it should be possible to estimate incident radiation. The opposite is also true, that given the incident radiation, the model with adjustments to match the max power point, should be able to estimate the performance of PV systems. With better understanding and more reliable information, the risks of deploying photovoltaic systems is reduced and the profits from PV systems will be determined with more reliability.

## VI. Acknowledgements

The University of Oregon Solar Radiation Monitoring Laboratory would like to thank the National Renewable Energy Laboratory as well as the Murdoch Family Trust for funding the project. We also thank the other sponsors of the University of Oregon Solar Radiation Monitoring Laboratory, the Bonneville Power Administration, the Energy Trust of Oregon, and Portland General Electric.

This work was authored in part by Alliance for Sustainable Energy, LLC, the manager and operator of the National Renewable Energy Laboratory for the U.S. Department of Energy (DOE) under Contract No. DE-AC36-08GO28308. Funding provided by U.S. Department of Energy Office of Energy Efficiency and Renewable Energy Solar Energy Technologies Office. The views expressed in the article do not necessarily represent the views of the DOE or the U.S. Government. The U.S. Government retains and the publisher, by accepting the article for publication, acknowledges that the U.S. Government retains a nonexclusive, paid-up, irrevocable, worldwide license to publish or reproduce the published form of this work, or allow others to do so, for U.S. Government purposes.

## References

[1] F. Vignola, J. Peterson, R. Kessler, S. Snider, P. Gotseff, M. Sengupta, A. Habte, A. Andreas, and F. Mavromatakis, "Influence of Diffuse and Ground-Reflected Irradiance on the Spectral Modeling of Solar Reference Cells," Proceedings of the American Solar Energy Society, Boulder, CO., 2021

[2] F. Vignola, J. Peterson, R. Kessler, S. Snider, A. Andreas, A. Habte, P. Gotseff, M. Sengupta, and F. Mavromatakis, "Evaluation of Reference Solar Cells on a Two-Axis Tracking Using Spectral Measurements," SolarPACES, September 27–October 1, 2020

[3] F. Vignola, J. Peterson, R. Kessler, V. Sandhu, S. Snider, A. Habte, P. Gotseff, A. Andreas, M. Sengupta, and F. Mavromatakis, "Improved Field Evaluation of Reference Cell Using Spectral Measurements," Solar Energy 215, (2021) pp. 482-491

[4] M. Sengupta, A. Habte, Y. Xie, P. Gotseff, M. Kutchenreiter, A. Afshin, I. Reda, F. Vignola, A. Driesse, C. Gueymard, S. Bandyopadhyay, and A. Denhard, "Solar Radiation Research Laboratory (SRRL) Final Report: Fiscal Years 2019–2021," 2022

[5] B. Marion, 2017. "Numerical method for angle-of-incidence correction factors for diffuse radiation incident photovoltaic modules," Solar Energy 147 344–348, 2017

[6] Y. Hishikawa, M. Yoshita, H. Ohshima, K. Yamagoe, H. Shimura, A. Sasaki, and T. Ueda, "Temperature dependence of the short circuit current and spectral responsivity of various kinds of crystalline silicon photovoltaic devices," Japanese Journal of Applied Physics 57, 08RG17 (2018)

[7] W. Marion and A. P. Dobos, "Rotation Angle for the Optimum Tracking of One-Axis Trackers," NREL/TP-6A20-58891 July 2013 https://www.nrel.gov/docs/fy13osti/58891.pdf].

[8] R. Perez, P. Ineichen, R. Seals, J. Michalsky, "Modeling daylight availability and irradiance components from direct and global irradiance," Solar Energy 44, 271–289, 1990